Nonlinear analysis of biaxially loaded rectangular concrete-filled stainless steel tubular slender beam-columns

Vipulkumar Ishvarbhai Patel[a], Qing Quan Liang[b],*, Muhammad N. S. Hadi[c]

[a] *School of Engineering and Mathematical Sciences, College of Science, Health and Engineering, La Trobe University, Bendigo, VIC 3552, Australia*
[b] *College of Engineering and Science, Victoria University, PO Box 14428, Melbourne, VIC 8001, Australia*
[c] *School of Civil, Mining and Environmental Engineering, University of Wollongong, Wollongong, NSW 2522, Australia*

ABSTRACT

Rectangular concrete-filled stainless steel tubular (CFSST) beam-columns utilized as supporting members for building frames may experience axial compression and biaxial moments. A numerical simulation considering the local buckling effects for thin-walled rectangular CFSST slender beam-columns has not been performed. This paper reports a stability modelling on the structural characteristics of rectangular CFSST slender beam-columns accounting for different strain-hardening of stainless steel under tension and compression. The influences of local buckling are considered in the simulation utilizing the existing effective width formulations. The developed numerical model simulates the strength interaction and load-deflection behavior of CFSST slender beam-columns. Comparisons of computed results with test data provided by experimental investigations are performed to validate the proposed fiber model. The influences of different geometric and material property on ultimate strengths, ultimate pure moments, concrete contribution ratio, strength interaction and load-deflection responses of CFSST slender beam-columns are examined by utilizing

*Corresponding author. Tel.: 61 3 9919 4134.
E-mail address: Qing.Liang@vu.edu.au (Q. Q. Liang)

fiber model. A design formula considering strain hardening of stainless steel is derived for calculating the ultimate pure moment of square CFSST beam-columns.

Keywords: Composite beam-columns; Fiber analysis; Local buckling; Numerical modeling; Progressive local buckling.

1. Introduction

Concrete-filled steel tubular (CFST) beam-columns have been extensively utilized as the compression members for electrical towers, caissons, piles and buildings in many countries [1]. This is attributed to the structural and constructional benefits offered by CFST slender beam-columns. The structural advantages include high elastic stiffness, ultimate strengths, ductility and large energy absorption capacity while the constructional advantages are rapid frame erection, significant reduction in materials, costs and section size and elimination of the plywood formworks [2]. The structural benefits depicted in Fig. 1 shows that the ultimate capacity of composite columns is higher than that of non-composite individual components. The use of stainless steels in CFST beam-columns provides additional advantages, including good corrosion resistance and aesthetic appearance [3-5]. Stainless steel has been used in landmark structures, such as the Hearst Tower in New York, the footbridges in Norway and Italy, the Stonecutters Bridge in Hong Kong and the Parliament House in Canberra [4]. Nevertheless, the initial high cost of stainless steels has restricted their use in general applications such as office or residential buildings. A life-cycle cost analysis needs to be utilized for the general application of concrete-filled stainless steel tubular (CFSST) beam-columns.

Rectangular CFSST beam-columns may experience axial compression and biaxial moments when they are located at the corners in composite buildings. The combined action of biaxial bending may also be caused by different bending moments transferred from the connecting composite beams. The stainless steel plates of biaxially loaded CFSST slender beam-column experience a stress gradient. The thin steel tube walls buckle locally outwards remarkably reducing the capacity of CFST columns [6-8]. The main failure of thin-walled slender CFSST columns can be described by local outward buckling and overall column buckling [9]. No numerical models with local buckling effects have been developed for the simulation of rectangular CFSST beam-columns supporting axial loading or axial compression and biaxial bending.

Extensive research studies have been devoted to the nonlinear characteristic of conventional CFST columns [10-16] while experimental investigations on slender CFSST beam-columns have been relatively limited. Previous studies by Young and Ellobody [17] showed that concentrically compressed rectangular CFSST short columns failed by local buckling of plates and concrete crushing. This test observation agrees with the experimental results reported by Lam and Gardner [18]. Uy et al. [9] tested twelve pin-ended rectangular and square CFSST slender columns under axial compression with different column slenderness ratios and concrete strengths to investigate their performance. As indicated, failure characteristic of slender columns was the global buckling with local buckling at their mid-length. Ellobody and Ghazy [19] tested circular CFSST slender beam-columns under eccentric loading. It was observed that most of the columns failed with gradually increasing the lateral deflections at the mid-length. Tokgoz [20] tested square CFSST slender beam-columns subjected to biaxial loads. Test results indicated that the ductility of high strength concrete was considerably increased due to the confinement offered by stainless steel tubes.

3

Nonlinear analysis methods have been employed to model the performance of CFST columns [21-32]. Nevertheless, a relatively limited number of studies have been devoted to the numerical simulation of CFSST beam-columns. The finite element analyses were performed by Ellobody and Young [33], Tao et al. [34] and Hassanein et al. [35, 36] to determine the deflections and strengths of square and circular CFSST short columns subjected to concentric loading. Although stainless steel has different strain-hardening behaviors in tension and compression, most of the analysis techniques employed material constitutive laws based on coupon tension tests to model the compressive behavior of CFSST columns. Ky et al. [37] developed a mathematical programming based algorithm utilizing the fiber element formulation and Müller's method for the inelastic analysis of axially loaded concrete encased composite short and slender columns. The mathematical model was shown to give good predictions of the behavior of concrete encased composite columns. Patel et al. [38, 39] reported that the material models of stainless steel in tension incorporated in the analysis underestimate the strengths of axially compressed CFSST short columns. Tokgoz [20] employed the fiber analysis technique to analyze biaxially loaded CFSST slender beam-columns with compact sections of stainless steel tubes.

The previous research studies indicate that limited experimental studies on rectangular CFSST slender beam-columns with biaxial loads have been performed. There have been few computational analyses on biaxially loaded CFSST slender beam-columns. Local buckling and different strain-hardening of stainless steel under compression and tension were not considered in the existing studies of rectangular CFSST slender beam-columns. A fiber model for analyzing the strength interaction and load-deflection behaviors of CFSST slender beam-columns is described herein. This model incorporates the influences of local buckling and strain-hardening of stainless steel tubes. Computational solutions are compared against test

4

data published by independent investigators. The influences of local buckling, concrete strengths, stainless steel strengths, depth-to-thickness ratios, slenderness ratios, eccentricity ratios and applied load angles on the nonlinear characteristic of CFSST beam-columns are discussed in detail. A simple formula is given for computing the ultimate pure moment of square CFSST beam-columns.

2. Material stress-strain relations

2.1. Concrete in compression

The concrete confinement increases the overall ductility of rectangular CFSST columns without increasing the strength. The increased ductility in the confined concrete is considered to accurately capture the performance of CFSST beam-columns. The constitutive law of concrete is represented by the nonlinear stress-strain relationship depicted in Fig. 2. This relationship contains a parabolic curve up to the concrete effective compressive strength f_{cc}', a constant portion at f_{cc}', a linear descending branch beyond f_{cc}' and constant residual strength after strain 0.015.

The four-stage stress-strain relations of concrete under compression illustrated in Fig. 2 were proposed by Liang [7] and are expressed by

$$\sigma_c = \begin{cases} \dfrac{f_{cc}'\lambda\left(\varepsilon_c/\varepsilon_{cc}'\right)}{\lambda-1+\left(\varepsilon_c/\varepsilon_{cc}'\right)^\lambda} & \text{for } 0 \leq \varepsilon_c \leq \varepsilon_{cc}' \\ f_{cc}' & \text{for } \varepsilon_{cc}' < \varepsilon_c \leq 0.005 \\ \beta_c f_{cc}' + 100(0.015-\varepsilon_c)\left(f_{cc}'-\beta_c f_{cc}'\right) & \text{for } 0.005 < \varepsilon_c \leq 0.015 \\ \beta_c f_{cc}' & \text{for } \varepsilon_c > 0.015 \end{cases} \qquad (1)$$

5

$$\lambda = \frac{E_c}{E_c - \left(f'_{cc} / \varepsilon'_{cc}\right)} \tag{2}$$

$$E_c = 3320\sqrt{\gamma_c f'_c} + 6900 \quad (\text{MPa}) \tag{3}$$

$$\varepsilon'_{cc} = \begin{cases} 0.002 & \text{for } f'_{cc} \leq 28 (\text{MPa}) \\ 0.002 + \dfrac{f'_{cc} - 28}{54000} & \text{for } 28 < f'_{cc} \leq 82 (\text{MPa}) \\ 0.003 & \text{for } f'_{cc} > 82 (\text{MPa}) \end{cases} \tag{4}$$

$$\beta_c = \begin{cases} 1.0 & \text{for } \dfrac{B_s}{t} \leq 24 \\ 1.5 - \dfrac{1}{48}\dfrac{B_s}{t} & \text{for } 24 < \dfrac{B_s}{t} \leq 48 \\ 0.5 & \text{for } \dfrac{B_s}{t} > 48 \end{cases} \tag{5}$$

$$\gamma_c = 1.85 D_c^{-0.135} \quad \left(0.85 \leq \gamma_c \leq 1.0\right) \tag{6}$$

in which σ_c represents the longitudinal stress, ε_c denotes the strain at σ_c, f'_{cc} stands for the effective compressive strength, ε'_{cc} denotes the strain corresponding to f'_{cc}, E_c represents the modulus of elasticity of concrete [40], f'_c stands for the cylinder strength of concrete in compression, γ_c denotes the factor given by Liang [7], D_c is the greater of $(B - 2t)$ and $(D - 2t)$, t stands for the thickness of stainless steel plate, B represents the width and D denotes the depth of rectangular cross-section, β_c stands for the strength degradation factor of concrete derived by Liang [7] for the post-peak characteristic of concrete, and B_s is the larger of width B and depth D. The geometric parameters B, D and t are shown in Fig. 3. The reduction factor γ_c accounts for the effects of column size, concrete quality and loading rate. This factor does not consider the increased ductility of the confined concrete as it has been incorporated in the stress-strain model for the confined concrete.

It is noted that the parabolic ascending curve of the compressive stress-strain relationship depicted in Fig. 2 is modeled using formulas given by Mander et al. [41]. The three linear branches as illustrated in Fig. 2 are formulated by Liang [7].

2.2. Concrete in tension

The concrete in tension exhibits the strain-softening and tension-stiffening behavior after cracking. These phenomena are characterized by a reduction in stress beyond the concrete tensile strength with an increase in the strain. The tension-stiffening behavior of concrete contributes to the overall stiffness of composite members after cracking. The material characteristics of concrete in tension with tension-stiffening and strain-softening as shown in Fig. 2 are considered herein. The stress proportionally increases with an increase in strain until concrete cracks. After reaching the strain at concrete tensile strength f_{ct}, the tensile concrete stress reduces linearly up to zero with increasing the strain. The stress in tension is taken as zero beyond the strain ε_{tu}. The strain ε_{tu} can be calculated by multiplying the factor 10 with the cracking strain ε_{tc}. The ultimate strength f_{ct} can be determined by $0.6\sqrt{\gamma_c f_c'}$.

2.3. Stainless steel in compression and tension

The constitutive model for stainless steel used in the numerical analysis could have a considerable impact on the computed results. Rasmussen [42] proposed a stress-strain relationship which assumes the same strain-hardening behavior for stainless steel in compression and tension. Quach et al. [43] and Abdella et al. [44] included the different stain-hardening behaviors of stainless steel under compression and tension in their three-stage stress-strain laws. The material laws were employed by Patel et al. [38, 39] in their

computational simulation of circular CFSST beam-columns. The three-stage stress-strain relations depicted in Fig. 4 are employed in the simulation of rectangular CFSST beam-columns, which are expressed by

$$
\sigma_s = \begin{cases} \dfrac{E_o\varepsilon_s\left(1+C_1\varepsilon_r^{C_2}\right)}{1+C_3\varepsilon_r^{C_4}+C_1\varepsilon_r^{C_2}} & \text{for } 0 \le \varepsilon_s \le \varepsilon_{0.2} \\[4mm] \sigma_{0.2}+\dfrac{E_{0.2}\varepsilon_*\left(1+C_5\varepsilon_{*r}^{C_6}\right)}{1+C_7\varepsilon_{*r}^{C_8}+C_5\varepsilon_{*r}^{C_6}} & \text{for } \varepsilon_{0.2} < \varepsilon_s \le \varepsilon_{2.0} \\[4mm] \dfrac{A_3+B_3\varepsilon_s}{1\pm\varepsilon_s} & \text{for } \varepsilon_s > \varepsilon_{2.0} \end{cases} \tag{7}
$$

in which σ_s represents the stainless steel stress, ε_s denotes the strain, E_0 is the modulus of elasticity, ε_r is taken as $\varepsilon_s/\varepsilon_{0.2}$, $\varepsilon_{0.2}$ is the 0.2% proof strain which is based on the model given by Ramberg and Osgood [45] and is given as

$$
\varepsilon_{0.2} = \frac{\sigma_{0.2}}{E_0}+0.002 \tag{8}
$$

In Eq. (7), C_1, C_2, C_3 and C_4 are the positive parameters. These constants are mathematically derived by Abdella et al. [44] and expressed by

$$
C_1 = \frac{\Delta}{C_2-1} \tag{9}
$$

$$
C_2 = 1+\frac{B_1}{\Delta} \tag{10}
$$

$$
C_3 = G_0\left(1+C_1\right) \tag{11}
$$

$$
C_4 = \Delta + G_1 \tag{12}
$$

8

where

$$\Delta = \frac{1 + \sqrt{1 + 4B_1}}{2} \tag{13}$$

$$B_1 = \frac{G_1 E_{0.2}(n + G_0)}{E_0} \tag{14}$$

$$G_0 = \frac{0.002 E_0}{\sigma_{0.2}} \tag{15}$$

$$G_1 = \frac{\varepsilon_{0.2} E_{0.2}(n - 1)}{\sigma_{0.2}} \tag{16}$$

$$E_{0.2} = \frac{E_0}{1 + 0.002\left(\dfrac{n E_0}{\sigma_{0.2}}\right)} \tag{17}$$

$$n = \frac{\ln(20)}{\ln(\sigma_{0.2}/\sigma_{0.1})} \tag{18}$$

where n represents the nonlinearity index proposed by Ramberg and Osgood [45] while $E_{0.2}$ represents the tangent modulus in Eq. (16).

For second stage of the stress-strain relation given in Eq. (7), $\sigma_{1.0}$ stands for the 1.0% proof stress and $\varepsilon_{1.0}$ represents the strain corresponding to the stress $\sigma_{1.0}$. The 1.0% proof stress and strain in compression and tension are computed by the formula proposed by Quach et al. [43] as

$$\sigma_{1.0} = \begin{cases} \sigma_{0.2}\left(\dfrac{0.662}{n}+1.085\right) & \text{for compression} \\ \sigma_{0.2}\left(\dfrac{0.542}{n}+1.072\right) & \text{for tension} \end{cases} \tag{19}$$

$$\varepsilon_{1.0} = \varepsilon_{0.2} + \frac{\sigma_{1.0}-\sigma_{0.2}}{E_{0.2}} + \left[0.008+\left(\sigma_{1.0}-\sigma_{0.2}\right)\left(\frac{1}{E_0}-\frac{1}{E_{0.2}}\right)\right] \tag{20}$$

The positive constants C_5, C_6, C_7 and C_8 shown in Eq. (7) are mathematically derived by

Abdella et al. [44] and are given by

$$C_5 = \frac{1}{C_6-1} \tag{21}$$

$$C_6 = C_8 + \frac{1}{\ln\left(\dfrac{\varepsilon_{2.0}-\varepsilon_{0.2}}{\varepsilon_{1.0}-\varepsilon_{0.2}}\right)}\left[\ln\left(1+A_2\right)+\ln\left(\frac{H_0}{H_2}\right)\right] \tag{22}$$

$$C_7 = H_0\left(1+C_5\right) \tag{23}$$

$$C_8 = 1 + H_1 \tag{24}$$

where

$$A_2 = \frac{\left(n_2-1\right)^2\left(H_2-H_0\right)}{\left(1+n_2H_0\right)\left(1+n_2H_2\right)} \tag{25}$$

$$H_0 = \frac{\left[0.008+\left(\sigma_{1.0}-\sigma_{0.2}\right)\left(\dfrac{1}{E_0}-\dfrac{1}{E_{0.2}}\right)\right]E_{0.2}}{\sigma_{1.0}-\sigma_{0.2}} \tag{26}$$

$$H_1 = \frac{\left(n_2-1\right)\left(H_0+1\right)}{1+n_2H_0} \tag{27}$$

$$H_2 = \frac{E_{0.2}\left(\dfrac{\varepsilon_{2.0} - \varepsilon_{0.2}}{\varepsilon_{1.0} - \varepsilon_{0.2}}\right)}{\sigma_{2.0} - \sigma_{0.2}} \tag{28}$$

where the parameter n_2 is given by Quach et al. [43] as follows:

$$n_2 = \begin{cases} 6.399\left(\dfrac{E_{0.2}}{E_0}\right)\left(\dfrac{\sigma_{1.0}}{\sigma_{0.2}}\right)+1.145 & \text{for compression} \\[2em] 12.255\left(\dfrac{E_{0.2}}{E_0}\right)\left(\dfrac{\sigma_{1.0}}{\sigma_{0.2}}\right)+1.037 & \text{for tension} \end{cases} \tag{29}$$

where $\sigma_{2.0}$ denotes the 2.0% proof stress and $\varepsilon_{2.0}$ stands for the strain corresponding to the stress $\sigma_{2.0}$. The 2.0% proof stress and strain are proposed by Quach et al. [43] as

$$\sigma_{2.0} = \sigma_{0.2}\left[\frac{1+\left(\dfrac{\sigma_{1.0}}{\sigma_{0.2}} - 1\right)A^{\frac{1}{n_2}}}{1+\left(\dfrac{\sigma_{0.2}}{E_0}\right)\left(\dfrac{E_0}{E_{0.2}} - 1\right)\left(\dfrac{\sigma_{1.0}}{\sigma_{0.2}} - 1\right)\left(\dfrac{A^{\frac{1}{n_2}}}{n_2 B_2}\right)}\right] \tag{30}$$

$$\varepsilon_{2.0} = \varepsilon_{0.2} + \frac{\sigma_{2.0} - \sigma_{0.2}}{E_{0.2}} + \left[0.008 + \left(\sigma_{1.0} - \sigma_{0.2}\right)\left(\frac{1}{E_0} - \frac{1}{E_{0.2}}\right)\right]\left(\frac{\sigma_{2.0} - \sigma_{0.2}}{\sigma_{1.0} - \sigma_{0.2}}\right)^{n_2} \tag{31}$$

where

$$A = \frac{B_2}{0.008 + \left(\dfrac{\sigma_{0.2}}{E_0}\right)\left(\dfrac{\sigma_{1.0}}{\sigma_{0.2}} - 1\right)\left(1 - \dfrac{E_0}{E_{0.2}}\right)} \tag{32}$$

11

$$B_2 = 0.018 + \left(\frac{\sigma_{0.2}}{E_0}\right)\left(\frac{E_0}{E_{0.2}} - 1\right) \tag{33}$$

In Eq. (7), the factors ε_* and ε_{*r} are given by Abdella et al. [44] as

$$\varepsilon_* = \varepsilon_s - \varepsilon_{0.2} \tag{34}$$

$$\varepsilon_{*r} = \frac{\varepsilon_*}{\varepsilon_s - \varepsilon_{0.2}} \tag{35}$$

For the third stage of formulation provided in Eq. (7), the negative and positive sign corresponds to the compression and tension, respectively.

In Eq. (7), A_3 and B_3 are material constants, which are computed by

$$A_3 = \sigma_{2.0}(1 + \varepsilon_{2.0}) - B_3\varepsilon_{2.0} \tag{36}$$

$$B_3 = \frac{\sigma_{su}(1 + \varepsilon_{su}) - \sigma_{2.0}(1 + \varepsilon_{2.0})}{\varepsilon_{su} - \varepsilon_{2.0}} \tag{37}$$

in which the ultimate strain ε_{su} and stress σ_{su} are determined by the equations presented by Quach et al. [43]:

$$\varepsilon_{uc} = 1 - \frac{1}{1 + \varepsilon_{ut}} \tag{38}$$

$$\sigma_{uc} = (1 + \varepsilon_{ut})^2 \sigma_{ut} \tag{39}$$

in which σ_{ut} represents the ultimate tensile strength while ε_{ut} denotes the strain at σ_{ut}, which are written as

$$\sigma_{ut} = \sigma_{0.2} \left[\frac{1 - 0.0375(n-5)}{185e + 0.2} \right] \tag{40}$$

$$\varepsilon_{ut} = 1 - \frac{\sigma_{0.2}}{\sigma_{ut}} \tag{41}$$

3. Fiber analysis

3.1. Basic concepts

The fiber analysis is used herein for analyzing the nonlinear behavior of rectangular CFSST beam-columns. In the fiber analysis, the column cross-section is first divided into steel and concrete elements as illustrated in Fig. 3. The stresses in these elements can then be predicted from the constitutive laws of stainless steel and concrete. The axial load and biaxial moments applied on the cross-section are determined by stress integration.

3.2. Simulation of cross-section under biaxial bending

The nonlinear behavior of CFSST beam-columns with thin-walled cross-sections is presented by the outward local buckling mode. Ineffective and effective widths of a plate with stress gradients are illustrated in Fig. 5. After exhibiting initial local buckling, the stainless steel tube walls under increasing compressive stresses undergo post-local buckling until the ultimate limit state is attained. The buckling of a stainless steel plate takes place in a progressive manner. The progressive local buckling performance is analyzed by gradually

13

redistributing in-plane stresses in the plate [7]. This post-local buckling of slender stainless steel cross-sections must be accounted for in the inelastic simulation of rectangular CFSST beam-columns.

The axial load-moment-curvature analysis can be utilized to compute the performance of biaxially loaded rectangular CFSST beam-columns. The maximum moment obtained from the complete moment-curvature response represents the ultimate bending strengths of the composite cross-section. For the given axial load with an angle (α) as depicted in Fig. 3, the moment-curvature relations are obtained through an incremental procedure in which the curvature is increased by steps. The moment capacity of the cross-section is solved for the corresponding curvature increment. The internal moments and axial forces are obtained from stress resultants which incorporate the influences of local buckling and different strain-hardening of stainless steel in compression and tension. For each curvature increment, neutral axis parameters, namely the depth d_n and orientation θ, are obtained by satisfying the force equilibrium $P_a - P = 0$ and moment equilibrium $\tan\alpha = M_y / M_x$, where P_a represents the applied axial load, α denotes the applied load angle measured at *y*-axis as shown in Fig. 3, and M_x and M_y stand for internal moments. The analysis steps for plotting moment-curvature responses are detailed by Liang [7].

Liang et al. [6] derived the effective width and strength formulas for carbon steel tubes in rectangular CFST columns. No study, however, is conducted on rectangular CFSST beam-columns incorporating local buckling of plates. For the evaluation of Liang et al. [6]'s formulas, the numerical predictions obtained from the fiber model are compared against the test data given by Uy et al. [9], Young and Ellobody [17] and Lam and Gardner [18] in Table 1, in which $P_{u.\text{fib}}$ stands for the ultimate axial strength obtained from the simulation, $P_{u.\text{exp}}$

denotes the experimental load and ε_u stands for the ultimate strain of CFSST short columns. As shown in Table 1, the fiber model employing the effective width formulas for the carbon steel plates reasonably predicts the ultimate loads of short CFSST columns. The predicted mean $P_{u.\mathrm{fib}}$-to-$P_{u.\exp}$ ratio is 0.97, which is close to unity and the corresponding standard deviation (SD) is 0.08 while the associated coefficient of variation (COV) is 0.09. The complete axial load-strain responses presented in Fig. 6 and Fig. 7(a) for CFSST short columns are also well captured by the fiber model including local buckling effects. The results presented herein demonstrate that the formulations given by Liang et al. [6] can be utilized for the simulation of rectangular CFSST columns.

3.3. Simulation of axial load-deflection curves

The computational algorithms given by Liang et al. [28] were used for the modeling of load-deflection response of CFSST slender beam-columns with biaxial loads. For inelastic stability simulation, the mid-length deflection u_m of a pin-ended beam-column is initialized. This deflection is gradually increased until the deflection limit is attained or the applied axial force is below the predefined strength limit. The mid-length curvature ϕ_m is determined from the mid-length deflection u_m. For each curvature, the neutral axis orientation and depth within the beam-column section are iteratively adjusted by employing Müller's numerical technique until moment equilibrium condition is attained at the mid-length of biaxially loaded columns. The internal axial load satisfying the moment equilibrium condition is determined as the applied axial load at the beam-column ends. A set of the axial loads and mid-length deflections obtained are utilized to define the complete axial load-deflection curve. Details on the theoretical formulas, equilibrium equations, and computational procedure for simulating axial load-deflection curves with local buckling effects are given by Liang et al. [28].

15

3.4. Simulation of load-moment interaction responses

The strength interaction in terms of axial load-moment $(P_n - M_n)$ responses for slender CFSST beam-columns can be utilized to examine the capacities against the design actions of axial compression and bending. This strength interaction depends on local buckling of plates, cross-sectional analysis, depth-to-thickness (D/t) ratios, eccentricity (e/D) ratios, slenderness (L/r) ratios, applied load angles (α), initial out-of-straightness, concrete compressive strengths (f_c') and stainless steel proof stress $(\sigma_{0.2})$, in which e denotes the loading eccentricity, r stands for the radius of gyration and L represents the length of beam-column.

For the analysis of strength interaction, the ultimate moment capacities are incrementally determined from given axial loads. The ultimate axial load (P_{oa}) of the slender CFSST columns under axial compression needs to be computed first utilizing the computational procedure described in Section 3.3. The applied load (P_n) is then gradually increased from 0 to $0.9P_{oa}$ with the load increment of $P_{oa}/10$. For each load increment, the mid-length curvature (ϕ_m) is progressively increased. The axial load-moment-curvature analysis procedure discussed in Section 3.2 is employed to compute the internal moment at the mid-length of biaxially loaded composite beam-columns. For each curvature increment, the end curvature (ϕ_e) is iteratively obtained using Müller's recursive algorithm and the corresponding end moment (M_e) is computed. For each load step, the bending strength (M_e) at the ends of the column is gradually incremented until the maximum end moment $(M_{e.max})$ is achieved. This maximum moment $(M_{e.max})$ can be found when external bending strength at

16

the mid-length (M_e) reaches the moment capacity of the cross-section for the given load. The maximum moments $(M_{e.max})$ and the axial loads can be utilized to draw the $P_n - M_n$ interaction diagram.

4. Verification of the fiber model

4.1. Comparison of ultimate axial strengths

The test data given by Uy et al. [9] on axially loaded square and rectangular CFSST slender columns were utilized to verify the fiber model. The results presented by Uy et al. [9] consist of 12 CFSST slender columns with D/t ratios of 36 and 52. Pin-ended conditions were adopted for all the columns. The slender columns were constructed using the stainless steel hollow sections filled with concrete strength of 36.3 MPa or 75.4 MPa. The austenitic stainless steel with proof stress of 363.3 MPa or 390.3 MPa was used to fabricate the hollow columns. The experimental ultimate axial loads ($P_{u.exp}$) and computed axial strengths ($P_{u.fib}$) are compared in Table 2. The mean ratio of $P_{u.fib}/P_{u.exp}$ and its SD and COV are 0.94, 0.05 and 0.05, respectively.

4.2. Comparison of load-deflection responses

The predicted axial load-deflection responses for axially loaded square and rectangular CFSST slender column are compared against the test data published by Uy et al. [9] in Fig. 7. The comparison indicates that the fiber analysis yields the accurate computation of the elastic stiffness of axially loaded CFSST slender columns. The difference between the axial loads of Specimens S1-1b and S1-2b in the post-peak range is within 10%. This discrepancy is mainly

due to the effects of average concrete strength utilized in the simulation. The axial load of Specimen S1-3b obtained from the fiber analysis in the post-yield range agrees closely with the experimental one. The developed fiber model is further verified by comparing computational results with test data on biaxially loaded square CFSST slender beam-columns given by Tokgoz [20] in Table 3. An initial geometric imperfection of $L/1000$ was considered in the numerical analyses. It should be noted that the beam-columns were not tested up to their ultimate strengths so Fig. 8 presents the comparisons of experimental initial stiffness with the complete numerical load-deflection curves. Good agreement between the computational and experimental load-deflection responses is obtained before the ultimate loads are reached. In conclusion, the fiber model accurately computes the elastic stiffness, ultimate axial strengths and displacement ductility of CFSST slender columns subjected to axial compression.

5. Behavior of CFSST slender beam-columns

The verified simulation procedure was employed to study the influences of local buckling, D/t ratio, L/r ratio, e/D ratio, applied load angle α, steel strength $\sigma_{0.2}$ and concrete cylinder strength f_c' on the performance of biaxially loaded beam-columns. The parametric investigation presented herein can be used for selecting the concrete strength f_c' in combination with the geometric properties such as L/r ratio, D/t ratio and e/D ratio. The following parametric study accounted for the imperfection in terms of out-of-straightness of $L/1000$ [39].

5.1. Ultimate axial strengths

Patel, V. I., Liang, Q. Q. and Hadi, M. N. S. (2017). Nonlinear analysis of biaxially loaded rectangular concrete-filled stainless steel tubular slender columns, *Engineering Structures*, 140:120-133.

The inelastic stability analysis was conducted on Specimen R1 given in Table 4 to simulate the influences of the D/t ratios, L/r ratios, e/D ratios and concrete strength f_c' on the ultimate axial loads. Fig. 9 illustrates the ultimate axial loads as a function of the e/D ratios which are varied from zero to two. As presented in Fig. 9, the ultimate load decreases as L/r ratio or e/D ratio increases. Nevertheless, increasing the steel tube thickness or concrete strength increases the axial strengths. Increasing concrete strength f_c' from 32 MPa to 100 MPa does not noticeably increase the ultimate loads of CFSST beam-columns having a large L/r ratio or a large e/D ratio when compared with CFSST short columns with a small e/D ratio.

5.2. Ultimate pure moments

The influences of various variables on the ultimate pure moments were studied using the developed fiber model. The Specimen R2 given in Table 4 was analyzed. The influences of D/t ratio on the ultimate pure moments are shown in Fig. 10, in which Z_e represents the elastic section modulus. As shown in Fig. 10, the ultimate pure moments decrease when the D/t ratio increases. This is because increasing D/t ratio reduces the steel area and plate buckling strength. The influences of concrete strength f_c' changing from 20 MPa to 120 MPa on ultimate pure moments are demonstrated in Fig. 11, where the factor γ_m depends on the D/t ratio which is proposed in Section 6. As depicted in Fig. 11, the ultimate pure moment increases as concrete strength f_c' increases. Fig. 12 presents the ultimate pure moment with different stainless steel proof stress $\sigma_{0.2}$. It appears that the ultimate pure moment increases

19

when the stainless steel strength $\sigma_{0.2}$ increases. The factor α_c depicted in Fig. 12 depends on the concrete strength f_c' and it is defined in Section 6.

5.3. Concrete contribution ratio $\left(\xi_c\right)$

The concrete strength can be selected for CFSST beam-columns using the concrete contribution ratio. This ratio is computed by $\xi_c = \left(P_n - P_s\right)/P_n$, in which P_n represents ultimate load of CFSST slender beam-columns which are loaded biaxially and P_s denotes the ultimate load of the stainless steel tubular beam-columns without concrete core [28]. The effects of e/D ratio, L/r ratio and strength f_c' on the concrete contribution ratio ξ_c were examined by undertaking the fiber analysis on Specimen R3 given in Table 4. The numerical results presented in Fig. 13 indicate that increasing the L/r ratio or e/D ratio with the same D/t ratio reduces the concrete contribution. A slender beam-column utilizing high strength concrete exhibits the most pronounced reduction in the concrete contribution. The benefits of high strength concrete can be achieved for CFSST beam-columns with small L/r ratios and e/D ratios. Therefore, high strength concrete can be used in CFSST beam-columns having a small L/r ratio, small e/D ratio and large D/t ratio.

5.4. Axial load-deflection responses

The effects of material and geometric parameters were examined by analyzing Specimen R4 listed in Table 4. It is seen from Fig. 14(a) that the local buckling of slender cross-section considerably reduces the capacity of CFSST slender beam-columns. As illustrated in Fig. 14, the initial stiffness and ultimate axial load decrease when the D/t ratio, L/r ratio or e/D

ratio increases but increase with increasing the concrete strength $f_c^{'}$ and stainless steel proof stress $\sigma_{0.2}$. On the other hand, the displacement ductility increases with increasing the D/t ratio, L/r ratio or e/D ratio but it decreases when the concrete strength $f_c^{'}$ increases. Fig. 14(d) shows the increasing axial load at mid-length deflection of 40 mm for the columns with e/D ratio of 0.3. This is due to the strain-hardening of stainless steel tubes which exhibits the higher load than the yield load [27]. As demonstrated in Fig. 14(f), the stiffness of axial load-deflection relation is not affected by the stainless steel strength $\sigma_{0.2}$.

5.5. Local buckling

The local buckling affects the nonlinear characteristic of rectangular CFST beam-columns [7, 8]. However, the influences of local buckling on the stiffness and axial capacity of CFSST beam-columns have not been reported. The fiber model was employed in the simulation of the Specimen R5 as provided in Table 4. The normalized ultimate axial load $\left(P_n/P_{oe}\right)$ with varying L/r ratios is illustrated in Fig. 15(a), where P_{oe} represents the ultimate strength of eccentrically loaded composite cross-section. The influence of local buckling on ultimate load of beam-column having zero length is the most pronounced. However, the influence of local buckling is found to decrease when the L/r ratio increases as illustrated in Fig. 15(a). The strength reduction of the beam-column with zero length due to local buckling is 10.3%. For a beam-column having the L/r ratio of 200, its ultimate load is decreased by only 1.1% owing to local buckling. This suggests that the strength of very slender CFSST beam-columns having L/r ratio greater than 200 is mainly governed by the overall column buckling and the local buckling effects can be ignored. As presented in Fig. 15(b), the ultimate strengths are

reduced considerably by local buckling. In Fig. 15(b), P_{oa} denotes the ultimate load of axially loaded slender columns, while M_o is the ultimate pure moment of beam-columns.

5.6. Applied load angle (α)

The influences of the applied load angle (α) on the strength of CFSST beam-columns were studied by utilizing the fiber analysis. A square CFSST slender Specimen R6 given in Table 4 was analyzed by varying the angle α from 0° to 90°. Fig. 16 illustrates the influences of angle α on the ultimate load of square CFSST beam-columns. As depicted in the figure, the ultimate load P_u of beam-columns is normalized by the ultimate load P_o of the cross-section loaded axially. The ultimate strain ε_u was assumed as 0.04 in the analysis of axially loaded column section. It reveals that increasing the angle α from 0° to 45° increases the ultimate load. Nevertheless, when increasing angle α from 45° to 90°, the ultimate axial load decreases. It should be noted that the influence of angle α on the ultimate axial strength is not significant as depicted in Fig. 16.

6. Design equation for ultimate pure moments

An equation for computing the ultimate pure moment (M_o) of CFST short beam-columns with circular section was derived by Liang and Fragomeni [46]. Their equation is extended for square CFSST short beam-columns including the influences of local buckling and different strain-hardening of stainless steel under tension and compression. The equation given by Liang and Fragomeni [46] is

$$M_o = \lambda_m \alpha_c \alpha_s Z_e \sigma_{0.2} \tag{42}$$

in which Z_e represents the elastic section modulus of a square CFSST beam-column, which is determined as $Z_e = \pi D^3 / 32$. Eq. (42) considers the influences of D/t ratios, concrete strength $f_c^{'}$ and stainless steel strength $\sigma_{0.2}$ using factors λ_m, α_c and α_s, respectively. The influences of local buckling and strain-hardening of stainless steel are accounted for in deriving these factors.

The results presented in Fig. 10 illustrate that the normalized strength $M_o / Z_e \sigma_{0.2}$ is reduced by increasing the D/t ratio. The factor λ_m is proposed using a nonlinear regression analysis by considering the influences of D/t ratios on strength M_o of square CFSST beam-columns. This factor λ_m is expressed as

$$\lambda_m = 0.0187 + 24.2 \left(\frac{t}{D} \right) - 61.1 \left(\frac{t}{D} \right)^2 \qquad \text{for} \, 10 \leq \frac{D}{t} \leq 120 \tag{43}$$

Fig. 11 presents the ratio of $M_o / Z_e \lambda_m \sigma_{0.2}$ as a function of concrete strength $f_c^{'}$. A nonlinear regression analysis is employed to obtain the following expression for the factor α_c:

$$\alpha_c = 0.7266 \left(f_c^{'} \right)^{0.0668} \qquad \text{for} \, 20 \leq f_c^{'} \leq 120 \, \text{MPa} \tag{44}$$

The effects of stainless steel proof stress $\sigma_{0.2}$ on the strength M_o are illustrated in Fig. 12. It is mentioned, the influences of concrete strength $f_c^{'}$ and D/t ratio were considered in the

factors α_c and λ_m in Fig. 12, respectively. The factor α_s is proposed for incorporating the effects of stainless steel strength $\sigma_{0.2}$ in the strength M_o of square CFSST beam-columns. The factor α_s is determined as

$$\alpha_s = 0.471 + \frac{262.62}{\sigma_{0.2}} - \frac{28119}{\sigma_{0.2}^2} \quad \text{for } 250 \leq \sigma_{0.2} \leq 690\,\text{MPa} \tag{45}$$

The proposed design equation for the strength M_o of square CFSST beam-columns is verified by comparing the calculated strengths using Eq. (42) with the numerical results obtained from the fiber model. Various D/t ratios, concrete strengths f_c' and stainless steel strengths $\sigma_{0.2}$ are considered in the verification of the design equation. The strength comparison is given in Table 5, in which $M_{o.\text{cal}}$ represents the ultimate pure moment predicted using Eq. (42) and $M_{o.\text{fib}}$ denotes the ultimate pure moment computed from fiber analysis. The comparison in Table 5 indicates that the mean value of $M_{o.\text{cal}}$-to-$M_{o.\text{fib}}$ ratio is 0.99 while SD and COV are 0.02. It is demonstrated that the design equation yields an accurate estimation of the strength M_o of square CFSST beam-columns.

7. Conclusions

This paper has reported a computational simulation on the stability modelling of rectangular CFSST slender beam-columns with axial compression and biaxial moments. This simulation accounts for the influences of different strain-hardening in tension and compression for stainless steel and locally buckled stainless steel plates on the characteristic of CFSST slender beam-columns. The fiber model proposed accurately predicts the experimentally observed

24

performance of CFSST slender columns. It has been revealed that the fiber model can be used to simulate the behavior of rectangular CFSST slender beam-columns. The parametric study has been carried out to examine influences of slenderness ratios, local buckling, loading eccentricities, depth-to-thickness ratios, applied load angle, stainless steel strengths and concrete strengths on the structural characteristic of CFSST slender beam-columns. A simple equation for computing the ultimate pure moments of square CFSST beam-columns considering the local buckling and strain hardening of steel has been proposed and compared with the prediction of the fiber model.

The numerical analysis reported in this paper leads to the following important conclusions:

- The local buckling of stainless steel tubes considerably reduces the stiffness, strength and ductility of thin-walled rectangular CFSST beam-columns. These effects must be considered in the analysis and design of thin-walled CFSST beam-columns.

- The ultimate loads of CFSST beam-columns considerably increase when the concrete strength increases, but remarkably decrease as the L/r ratio, D/t ratio or e/D ratio increases.

- For slender CFSST beam-columns with a large e/D ratio or a large L/r ratio, it is effective to increase the steel areas or use high strength stainless steel to increase their ultimate axial strengths.

- The concrete contribution ratio ξ_c is significantly increased by increasing the concrete strength or D/t ratio. However, it is decreased by increasing the e/D ratio or L/r ratio.

- For CFSST beam-columns with a large e/D ratio or a large L/r ratio, it is not effective to use high strength concrete to increase their ultimate axial strengths.

Patel, V. I., Liang, Q. Q. and Hadi, M. N. S. (2017). Nonlinear analysis of biaxially loaded rectangular concrete-filled stainless steel tubular slender columns, *Engineering Structures*, 140:120-133.

- When a CFSST slender beam-column having a large D/t ratio, a small L/r ratio and a small e/D ratio, high strength concrete should be utilized to increase its ultimate axial strength. It means that it is more effective to utilize high strength concrete to increase the ultimate axial load of section or intermediate length columns rather than very slender columns.

- The D/t ratio has pronounced effects on the section capacity rather than the column capacity.

- The e/D and L/r ratios have pronounced effects on the column axial strength rather than the section axial capacity.

- The loading angle has little influence on the ultimate loads of CFSST beam-columns.

- The proposed design equation accurately computes the ultimate pure moments of square CFSST beam-columns.

References

[1]   Han LH, Li W, Bjorhovde R. Developments and advanced applications of concrete-filled steel tubular (CFST) structures: Members. J Constr Steel Res 2014;100:211-28.

[2]   Patel VI, Liang QQ, Hadi MNS. Nonlinear analysis of concrete-filled steel tubular columns. Germany: Scholars' press; 2015.

[3]   Mann AP. The structural use of stainless steel. The Structural Engineer 1993;71(4):60-9.

[4]   Baddoo NR. Stainless steel in construction: A review of research, applications, challenges and opportunities. J Constr Steel Res 2008;64(11):1199-1206.

[5]   Gardner L. Aesthetics, economics and design of stainless steel structures. Adv Steel Constr 2008;4(2):113-22.

Patel, V. I., Liang, Q. Q. and Hadi, M. N. S. (2017). Nonlinear analysis of biaxially loaded rectangular concrete-filled stainless steel tubular slender columns, *Engineering Structures*, 140:120-133.

[6]   Liang QQ, Uy B, Liew JYR. Local buckling of steel plates in concrete-filled thin-walled steel tubular beam-columns. J Constr Steel Res 2007;63(3):396-405.

[7]   Liang QQ. Performance-based analysis of concrete-filled steel tubular beam-columns, Part I: Theory and algorithms. J Constr Steel Res 2009;65(2):363-72.

[8]   Liang QQ. Performance-based analysis of concrete-filled steel tubular beam-columns, Part II: Verification and applications. J Constr Steel Res 2009;65(2):351-62.

[9]   Uy B, Tao Z, Han LH. Behaviour of short and slender concrete-filled stainless steel tubular columns. J Constr Steel Res 2011;67(3):360-78.

[10] Shakir-Khalil H, Zeghiche J. Experimental behaviour of concrete-filled rolled rectangular hollow-section columns. The Structural Engineer 1989;67(19):346-53.

[11] Schneider SP. Axially loaded concrete-filled steel tubes. J Struct Eng ASCE 1998;124(10):1125-38.

[12] Varma AH, Ricles JM, Sause R, Lu LW. Seismic behavior and modelling of high-strength composite concrete-filled steel tube (CFT) beam-columns. J Constr Steel Res 2002;58(5-8):725-58.

[13] Mursi M, Uy B. Behaviour and design of fabricated high strength steel columns subjected to biaxial bending. Part I: Experiments. Adv Steel Constr 2006;2(4):286-315.

[14] Liu D. Behaviour of eccentrically loaded high-strength rectangular concrete-filled steel tubular columns. J Constr Steel Res 2006;62(8):839-46.

[15] Portolés JM, Romero ML, Bonet JL, Filippou FC. Experimental study of high strength concrete-filled circular tubular columns under eccentric loading. J Constr Steel Res 2011;67(4):623-33.

[16] Dundu M. Column buckling tests of hot-rolled concrete filled square hollow sections of mild to high strength steel. Eng Struct 2016;127:73-85.

[17] Young B, Ellobody E. Experimental investigation of concrete-filled cold-formed high strength stainless steel tube columns. J Constr Steel Res 2006;62(5):484-92.

[18] Lam D, Gardner L. Structural design of stainless steel concrete filled columns. J Constr Steel Res 2008;64(11):1275-82.

[19] Ellobody E, Ghazy MF. Experimental investigation of eccentrically loaded fiber reinforced concrete-filled stainless steel tubular columns. J Constr Steel Res 2012;76:167-76.

[20] Tokgoz S. Tests on plain and steel fiber concrete-filled stainless steel tubular columns. J Constr Steel Res 2015;114:129-35.

[21] Hajjar JF, Schiller PH, Molodan A. A distributed plasticity model for concrete-filled steel tube beam-columns with interlayer slip. Eng Struct 1998;20(8):663-76.

[22] Susantha KAS, Ge HB, Usami T. Uniaxial stress-strain relationship of concrete confined by various shaped steel tubes. Eng Struct 2001;23(10):1331-47.

[23] Shanmugam NE, Lakshmi B, Uy B. An analytical model for thin-walled steel box columns with concrete in-fill. Eng Struct 2002;24(6):825-38.

[24] Mursi M, Uy B. Behaviour and design of fabricated high strength steel columns subjected to biaxial bending. Part II: Analysis and design codes. Adv Steel Constr 2006;2(4):286-315.

[25] Portolés JM, Romero ML, Filippou FC, Bonet JL. Simulation and design recommendations of eccentrically loaded slender concrete-filled tubular columns. Eng Struct 2011;33(5):1576-93.

[26] Patel VI, Liang QQ, Hadi MNS. High strength thin-walled rectangular concrete-filled steel tubular slender beam-columns. Part I: Modeling. J Constr Steel Res 2012;70:377-84.

[27] Patel VI, Liang QQ, Hadi MNS. High strength thin-walled rectangular concrete-filled steel tubular slender beam-columns. Part II: Behavior. J Constr Steel Res 2012;70:368-76.

[28] Liang QQ, Patel VI, Hadi MNS. Biaxially loaded high-strength concrete-filled steel tubular slender beam-columns, Part I: Multiscale simulation. J Constr Steel Res 2012;75:64-71.

[29] Ellobody E. Nonlinear behaviour of eccentrically loaded FR concrete-filled stainless steel tubular columns. J Constr Steel Res 2013;90:1-12.

[30] Mollazadeh MH, Wang YC. New insights into the mechanism of load introduction into concrete-filled steel tubular column through shear connection. Eng Struct 2014;75:139-51.

[31] Patel VI, Liang QQ, Hadi MNS. Biaxially loaded high-strength concrete-filled steel tubular slender beam-columns, Part II: Parametric study. J Constr Steel Res 2015;110:200-07.

[32] Lai Z, Varma AH. Effective stress-strain relationships for analysis of noncompact and slender filled composite (CFT) members. Eng Struct 2016;124:457-72.

[33] Ellobody E, Young B. Design and behaviour of concrete-filled cold-formed stainless steel tube columns. Eng Struct 2006;28(5):716-28.

[34] Tao Z, Uy B, Liao FY, Han LH. Nonlinear analysis of concrete-filled square stainless steel stub columns under axial compression. J Constr Steel Res 2011;67(11):1719-32.

[35] Hassanein MF, Kharoob OF, Liang QQ. Behaviour of circular concrete-filled lean duplex stainless steel tubular short columns. Thin-Walled Struct 2013;68:113-23.

[36] Hassanein MF, Kharoob OF, Liang QQ. Behaviour of circular concrete-filled lean duplex stainless steel-carbon steel tubular short columns. Eng Struct 2013;56:83-94.

[37] Ky VS, Tangaramvong S, Thepchatri T. Inelastic analysis for the post-collapse behavior of concrete encased steel composite columns under axial compression. Steel Compos Struct 2015;19(5):1237-58.

[38] Patel VI, Liang QQ, Hadi MNS. Nonlinear analysis of axially loaded circular concrete-filled stainless steel tubular short columns. J Constr Steel Res 2014;101:9-18.

[39] Patel VI, Liang QQ, Hadi MNS. Nonlinear analysis of circular high strength concrete-filled stainless steel tubular slender beam-columns. Eng Struct 2017;130:1-13.

[40] ACI Committee 363. State of the Art Report on High-Strength Concrete, ACI Publication 363R-92, Detroit, MI: American Concrete Institute, 1992.

[41] Mander JB, Priestly MNJ, Park R. Theoretical stress-strain model for confined concrete. J Struct Eng, ASCE 1988;114(8):1804-26.

[42] Rasmussen KJR. Full-range stress-strain curves for stainless steel alloys. J Constr Steel Res 2003;59(1):47-61.

[43] Quach WM, Teng JG, Chung KF. Three-stage full-range stress-strain model for stainless steels. J Struct Eng, ASCE 2008;134(9):1518-27.

[44] Abdella K, Thannon RA, Mehri AI, Alshaikh FA. Inversion of three-stage stress-strain relation for stainless steel in tension and compression. J Constr Steel Res 2011;67(5):826-32.

[45] Ramberg W, Osgood WR. Description of stress-strain relations from offset yield strength values. NACA Technical Note no. 927, 1944.

[46] Liang QQ, Fragomeni S. Nonlinear analysis of circular concrete-filled steel tubular short columns under eccentric loading. J Constr Steel Res 2010;66(2):159-69.

Figures and tables

Table 1 Ultimate axial loads of rectangular CFSST short columns under axial compression.

Specimens	$B \times D \times t$ (mm)	D/t	f_c' (MPa)	$\sigma_{0.2}$ (MPa)	E_0 (GPa)	n	ε_u	$P_{u.exp}$ (kN)	$P_{u.fib}$ (kN)	$\dfrac{P_{u.fib}}{P_{u.exp}}$	Ref.
RHS3C40	80.1 × 140.2 × 3.1	45	46.6	486	212.0	6	0.025	1048.7	1039	0.99	
RHS3C60	80.1 × 140.2 × 3.1	45	61.9	486	212.0	6	0.025	1096.9	1184	1.08	[17]
RHS3C80	80.0 × 140.3 × 3.1	45	83.5	486	212.0	6	0.015	1258.8	1389	1.10	
SHS 100 × 100 × 2 - C30	101.6 × 100.2 × 2.2	46	30	385	202.5	12.4	0.041	534	564	1.06	[18]
SHS 100 × 100 × 2 - C60	99.3 × 101.3 × 2	51	53	385	202.5	12.4	0.05	687	744	1.08	
S20-50 × 2A	51 × 51 × 1.81	28	21.5	353	205.1	10.4	0.066	261	233	0.89	
S20-50 × 2B	51 × 51 × 1.81	28	21.5	353	205.1	10.4	0.064	256	231	0.90	
S30-50 × 2A	51 × 51 × 1.81	28	34.9	353	205.1	10.4	0.095	282	280	0.99	
S30-50 × 2B	51 × 51 × 1.81	28	34.9	353	205.1	10.4	0.065	278	259	0.93	
S20-50 × 3B	51 × 51 × 2.85	18	21.5	440	207.9	8.2	0.099	417	445	1.07	
S30-100 × 3A	100 × 100 × 2.85	35	34.9	358	195.7	8.3	0.0047	765	661	0.86	
S30-100 × 3B	100 × 100 × 2.85	35	34.9	358	195.7	8.3	0.057	742	661	0.89	
S20-100 × 5A	101 × 101 × 5.05	20	21.5	435	202.1	7	0.029	1437	1288	0.90	[9]
S20-100 × 5B	101 × 101 × 5.05	20	21.5	435	202.1	7	0.029	1449	1288	0.89	
S30-100 × 5A	101 × 101 × 5.05	20	34.9	435	202.1	7	0.054	1474	1506	1.02	
S30-100 × 5B	101 × 101 × 5.05	20	34.9	435	202.1	7	0.027	1490	1390	0.93	
S30-150 × 3A	152 × 152 × 2.85	53	34.9	268	192.6	6.8	0.0015	1074	965	0.90	
S30-150 × 3B	152 × 152 × 2.85	53	34.9	268	192.6	6.8	0.0029	1209	1082	0.89	
S20-150 × 5B	150 × 150 × 4.8	31	21.5	340	192.2	5.6	0.1	1935	2092	1.08	
S30-150 × 5A	150 × 150 × 4.8	31	34.9	340	192.2	5.6	0.066	2048	2073	1.01	
Mean										0.97	
Standard deviation (SD)										0.08	
Coefficient of variation (COV)										0.09	

Table 2 Ultimate axial loads of rectangular CFSST slender columns under axial compression.

Specimens	$B \times D \times t$ (mm)	D/t	L (mm)	$\sigma_{0.2}$ (MPa)	E_0 (GPa)	n	f_c' (MPa)	$P_{u.exp}$ (kN)	$P_{u.fib}$ (kN)	$\dfrac{P_{u.fib}}{P_{u.exp}}$	Ref.
S1-1a	100.3 × 100.3 × 2.76	36	440	390.3	182.0	6.7	36.3	767..6	696.4	0.91	
S1-1b	100.3 × 100.3 × 2.76	36	440	390.3	182.0	6.7	75.4	1090.5	1046.4	0.96	
S1-2a	100.3 × 100.3 × 2.76	36	1340	390.3	182.0	6.7	36.3	697.3	657.5	0.94	
S1-2b	100.3 × 100.3 × 2.76	36	1340	390.3	182.0	6.7	75.4	1022.9	987.5	0.97	
S1-3a	100.3 × 100.3 × 2.76	36	2540	390.3	182.0	6.7	36.3	622.9	529.5	0.85	
S1-3b	100.3 × 100.3 × 2.76	36	2540	390.3	182.0	6.7	75.4	684.2	700.7	1.02	[9]
R1-1a	49.0 × 99.5 × 1.93	52	440	363.3	195.3	6.1	36.3	385.6	339.9	0.88	
R1-1b	49.0 × 99.5 × 1.93	52	440	363.3	195.3	6.1	75.4	558.3	508.1	0.91	
R1-2a	49.0 × 99.5 × 1.93	52	740	363.3	195.3	6.1	36.3	361.1	335.4	0.93	
R1-2b	49.0 × 99.5 × 1.93	52	740	363.3	195.3	6.1	75.4	517.7	500.1	0.97	
R1-3a	49.0 × 99.5 × 1.93	52	2540	363.3	195.3	6.1	36.3	262.8	247.7	0.94	
R1-3b	49.0 × 99.5 × 1.93	52	2540	363.3	195.3	6.1	75.4	332.8	322.6	0.97	
Mean										0.94	
Standard deviation (SD)										0.05	
Coefficient of variation (COV)										0.05	

Patel, V. I., Liang, Q. Q. and Hadi, M. N. S. (2017). Nonlinear analysis of biaxially loaded rectangular concrete-filled stainless steel tubular slender columns, *Engineering Structures*, 140:120-133.

Table 3 Square CFSST slender beam-columns under axial compression and biaxial bending.

Specimens	$B{\times}D{\times}t$ (mm)	D/t	L (mm)	e_x (mm)	e_y (mm)	f_c' (MPa)	$\sigma_{0.2}$ (MPa)	E_0 (GPa)	Ref.
CFSSTC-I	$60 \times 60 \times 3$	20	1200	30	30	40.14	650	200	
	$80 \times 80 \times 3$	27	1200	40	40	40.14	650	200	
CFSSTC-II	$60 \times 60 \times 3$	20	1200	35	35	54.32	650	200	[20]
	$80 \times 80 \times 3$	27	1200	45	45	54.32	650	200	
CFSSTC-III	$60 \times 60 \times 3$	20	1200	45	45	58.42	650	200	
	$100 \times 100 \times 3$	33	1200	65	65	58.42	650	200	

Table 4 Material properties and geocentric details of CFSST slender beam-columns for parametric study.

Specimens	$B{\times}D$ (mm)	D/t	$\alpha(^\circ)$	e/D	L/r	$\sigma_{0.2}$ (MPa)	E_0 (GPa)	n	f_c' (MPa)
R1	500×500	100	30	0.1	100	390	182	7	100
R2	400×400	100	60	0.1	22	340	192	6	100
R3	500×600	100	45	0.1	100	490	212	6	100
R4	650×650	80	30	0.1	35	340	192	6	65
R5	700×700	100	60	0.1	22	360	195	6	65
R6	600×600	25	45	0.1	22	430	202	7	80

Table 5 Ultimate pure moments of square CFSST short beam-columns.

| Specimens	$B \times D \times t$ (mm)	D/t	$\sigma_{0.2}$ (MPa)	E_0 (GPa)	n	f_c' (MPa)	$M_{o.\text{cal}}$ (kNm)	$M_{o.\text{fib}}$ (kNm)	$\dfrac{M_{o.\text{cal}}}{M_{o.\text{fib}}}$
S1	$300 \times 300 \times 5.00$	60	250	200	7	20	256	259	0.99
S2	$300 \times 300 \times 5.00$	60	250	200	7	25	260	262	0.99
S3	$300 \times 300 \times 5.00$	60	250	200	7	32	264	266	0.99
S4	$300 \times 300 \times 5.00$	60	250	200	7	65	277	282	0.98
S5	$300 \times 300 \times 5.00$	60	250	200	7	80	281	288	0.97
S6	$300 \times 300 \times 5.00$	60	250	200	7	100	285	295	0.97
S7	$300 \times 300 \times 5.00$	60	300	200	7	80	325	329	0.99
S8	$300 \times 300 \times 5.00$	60	400	200	7	80	399	388	1.03
S9	$300 \times 300 \times 5.00$	60	550	200	7	80	493	511	0.96
S10	$300 \times 300 \times 6.00$	50	250	200	7	65	327	307	1.06
S11	$300 \times 300 \times 4.29$	70	250	200	7	65	241	247	0.97
S12	$300 \times 300 \times 3.75$	80	250	200	7	65	213	220	0.97
S13	$300 \times 300 \times 3.33$	90	250	200	7	65	191	199	0.96
S14	$300 \times 300 \times 3.00$	100	250	200	7	65	174	182	0.96
S15	$500 \times 500 \times 10.00$	50	300	200	7	20	1618	1638	0.99
S16	$500 \times 500 \times 10.00$	50	300	200	7	25	1643	1652	0.99
S17	$500 \times 500 \times 10.00$	50	300	200	7	32	1670	1670	1.00
S18	$500 \times 500 \times 10.00$	50	300	200	7	40	1695	1691	1.00
S19	$500 \times 500 \times 10.00$	50	300	200	7	50	1721	1715	1.00
S20	$500 \times 500 \times 10.00$	50	300	200	7	80	1775	1780	1.00
S21	$500 \times 500 \times 10.00$	50	300	200	7	100	1802	1818	0.99
S22	$500 \times 500 \times 10.00$	50	250	200	7	100	1556	1590	0.98
S23	$500 \times 500 \times 10.00$	50	350	200	7	100	2017	2037	0.99
S24	$500 \times 500 \times 10.00$	50	550	200	7	100	2734	2721	1.00
S25	$500 \times 500 \times 8.33$	60	450	200	7	50	1935	1983	0.98
S26	$500 \times 500 \times 7.69$	65	450	200	7	50	1799	1845	0.98
S27	$500 \times 500 \times 6.25$	80	450	200	7	50	1489	1533	0.97
S28	$500 \times 500 \times 5.56$	90	450	200	7	50	1339	1380	0.97
S29	$500 \times 500 \times 5.00$	100	450	200	7	50	1217	1257	0.97
S30	$600 \times 600 \times 10.00$	60	300	200	7	80	2598	2631	0.99
S31	$700 \times 700 \times 10.00$	70	300	200	7	80	3585	3662	0.98
S32	$800 \times 800 \times 10.00$	80	300	200	7	80	4739	4877	0.97
S33	$900 \times 900 \times 10.00$	90	300	200	7	80	6063	6280	0.97
Mean									0.99
Standard deviation (SD)									0.02
Coefficient of variation (COV)									0.02
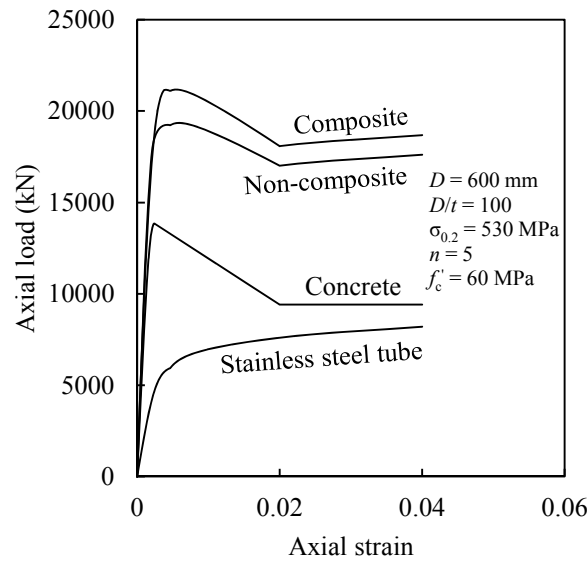
Fig. 1. Component strengths of axially loaded circular CFSST short column.
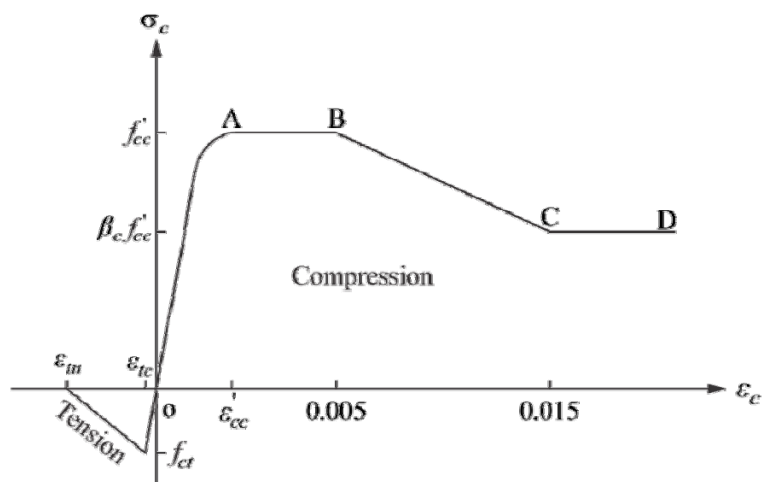

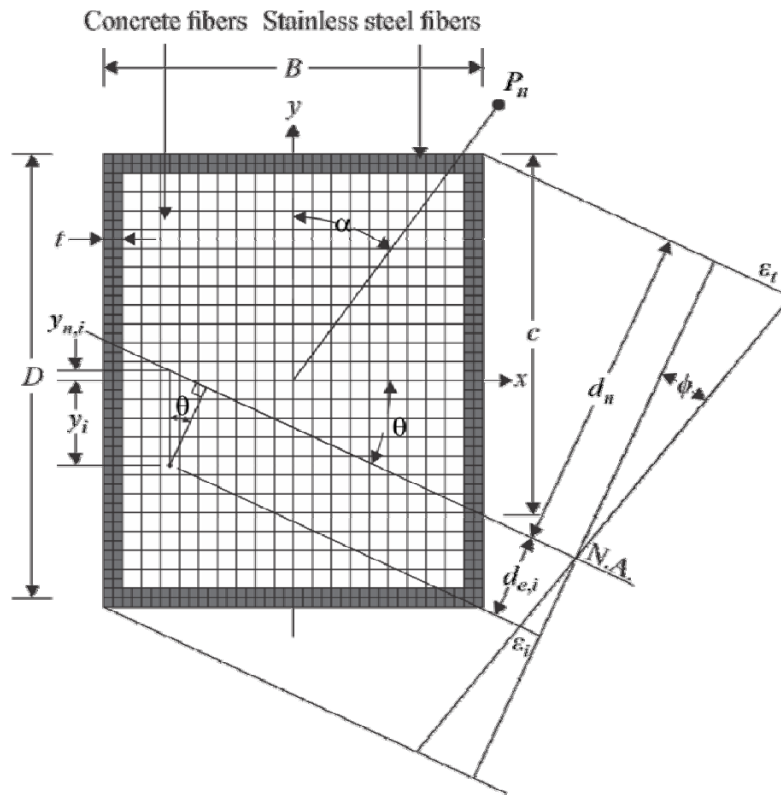**Fig. 2.** Typical stress-strain curves for concrete.

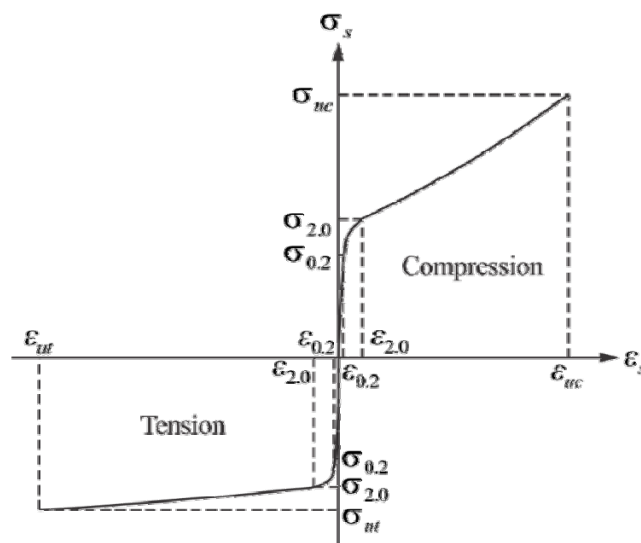**Fig. 3.** Rectangular cross-section of a CFSST beam-column with fiber elements.

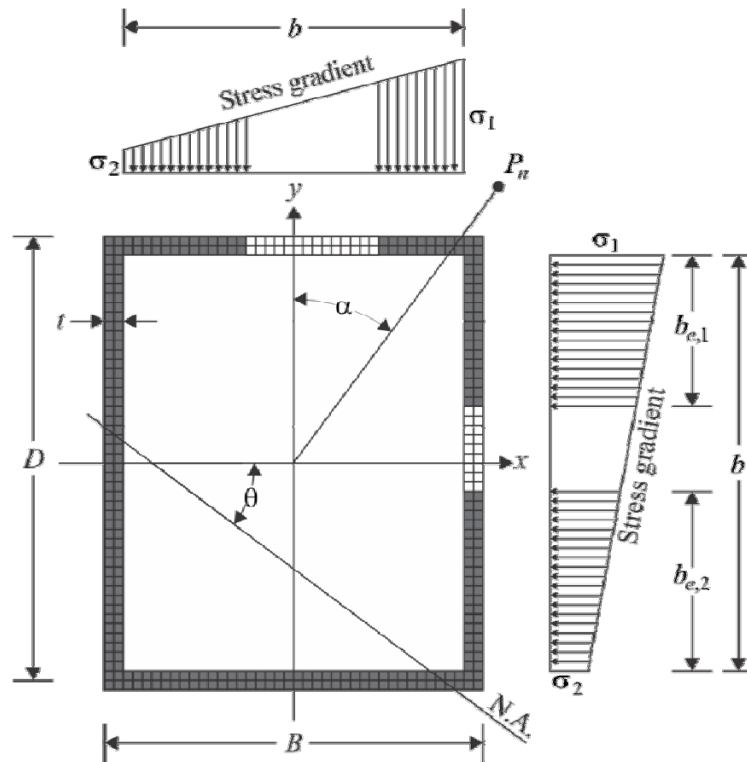**Fig. 4.** Full-range stress-strain curves for stainless steel.

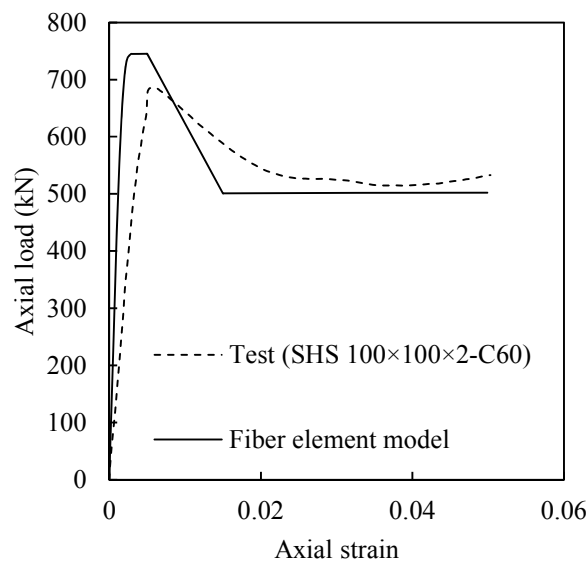**Fig. 5.** Effective areas of webs and flanges of rectangular CFSST column section.

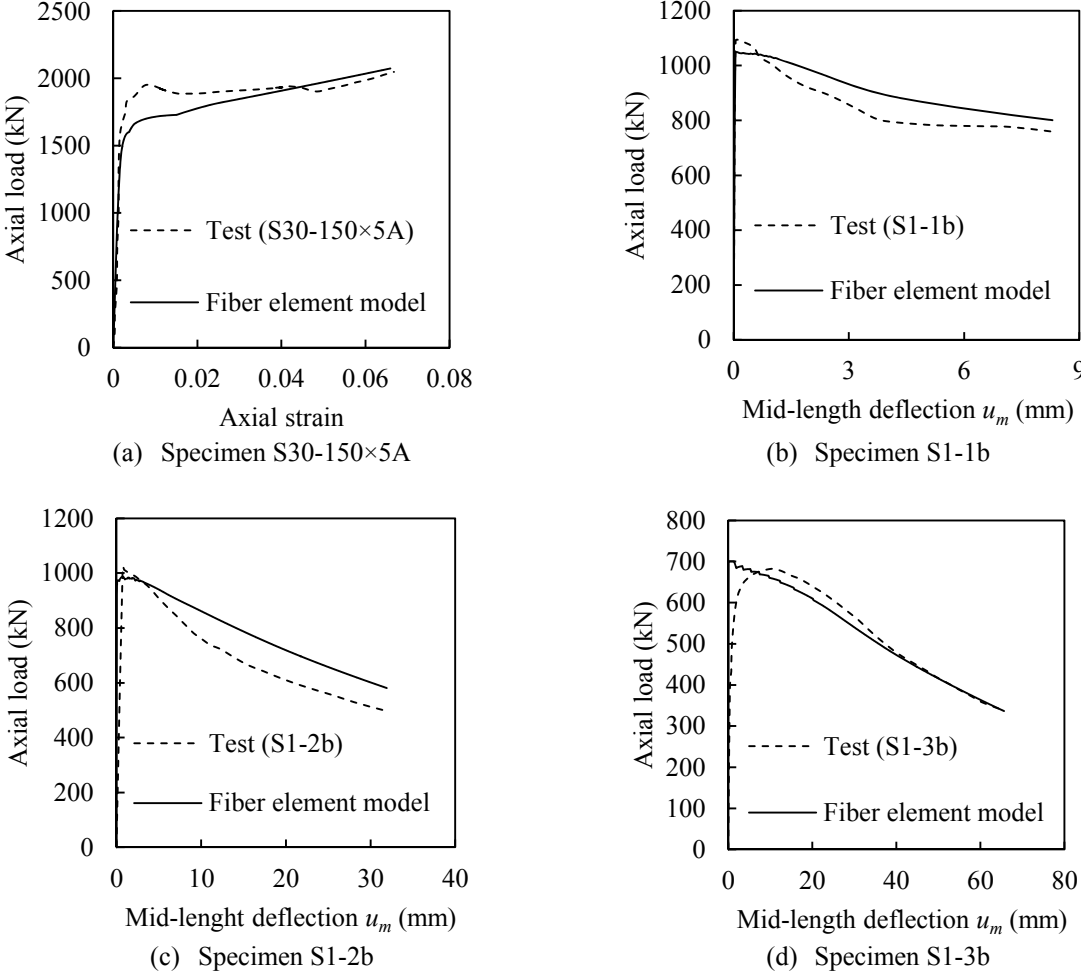**Fig. 6.** Comparison of axial load-strain responses for the specimen tested by Lam et al. [18].

Fig. 7. Comparison of predicted and experimental reponses for specimens tested by Uy et al. [9].

(a) Specimen I-60×60×3

(b) Specimen I-80×80×3

(c) Specimen II-60×60×3

(d) Specimen II-80×80×3

(e) Specimen III-60×60×3

(f) Specimen III-100×100×3
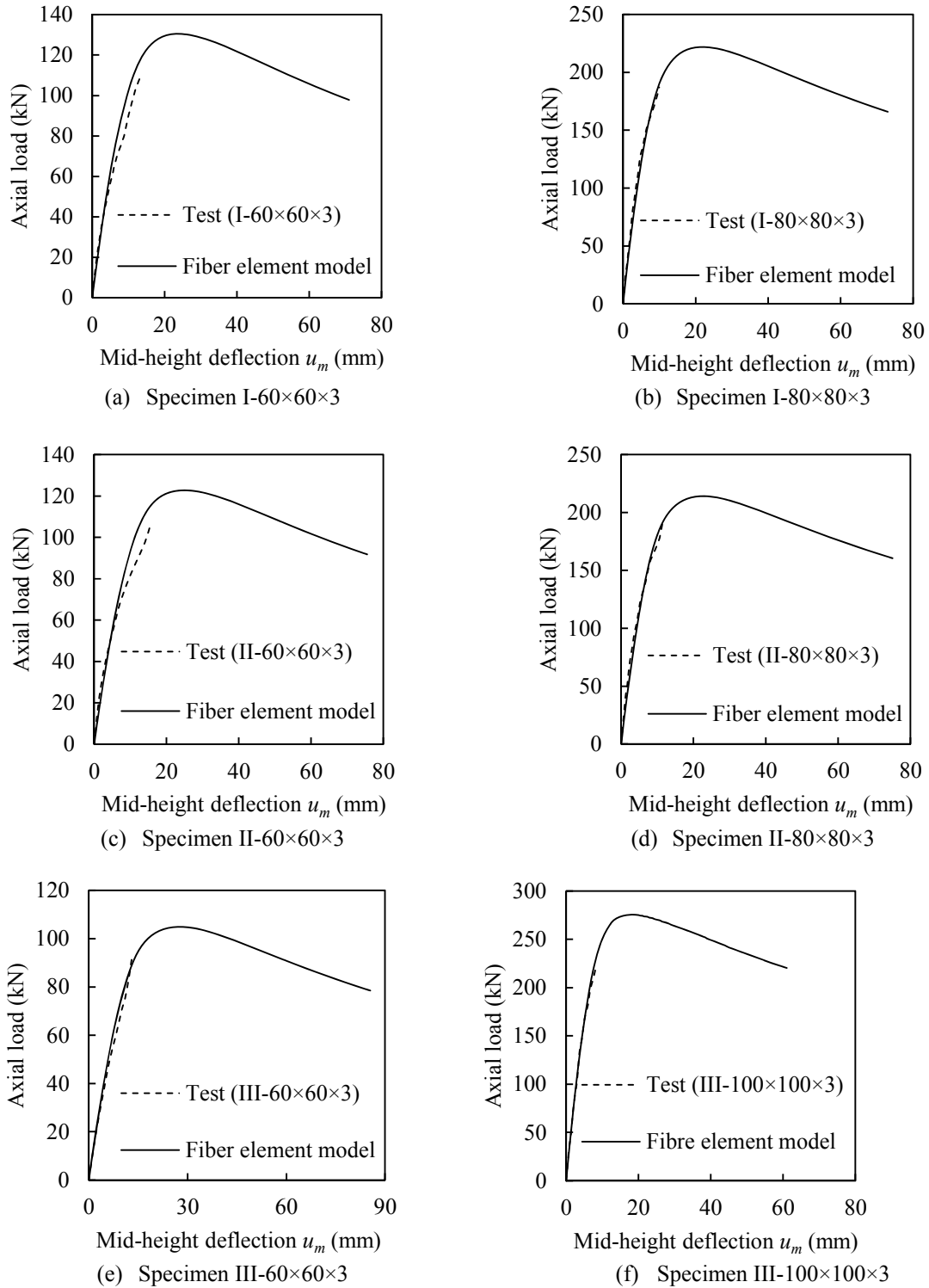
Fig. 8. Comparison of predicted and measured load-deflection curves for specimens tested by Tokgoz [20].

(a) D/t ratio = 50

(b) D/t ratio = 100
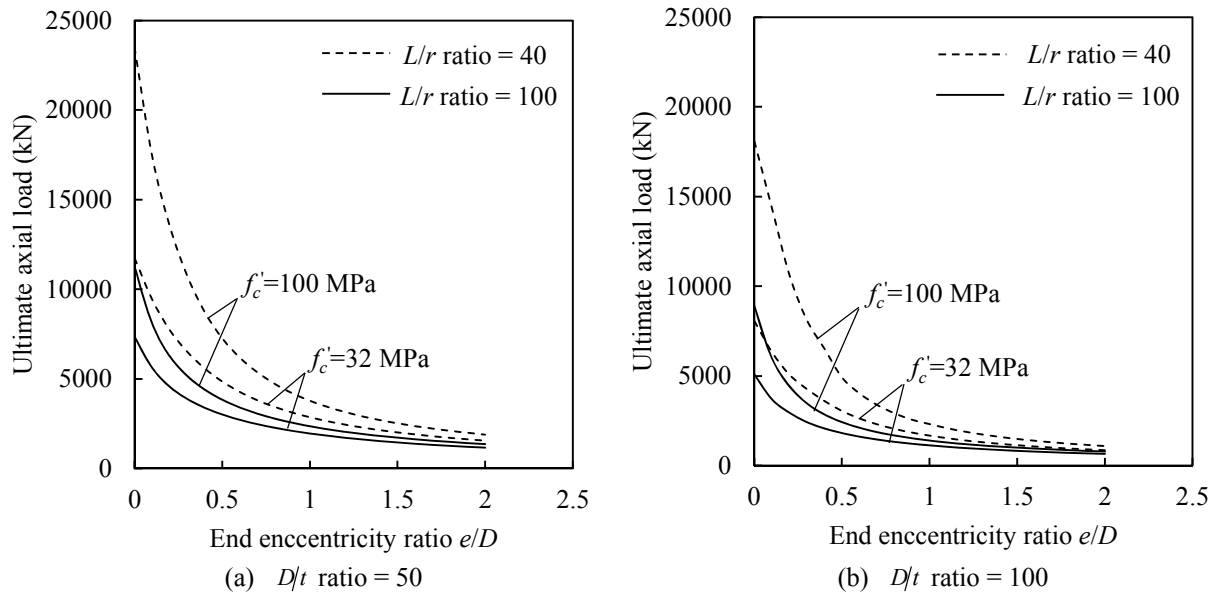
Fig. 9. Influences of geometric and material parameters on the ultimate axial loads.
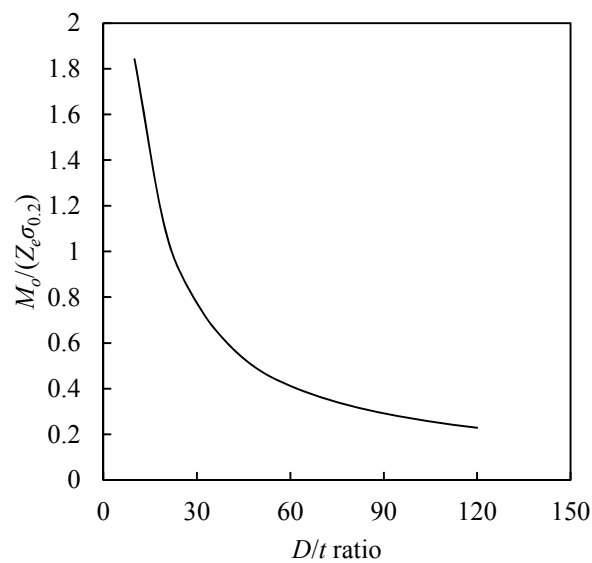
Fig. 10. Influences of D/t ratio on the ultimate pure moment.
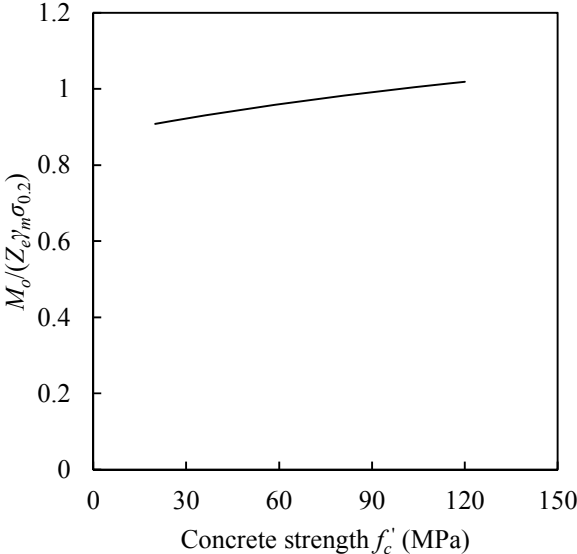
Fig. 11. Influences of concrete strength f_c' on the ultimate pure moment.
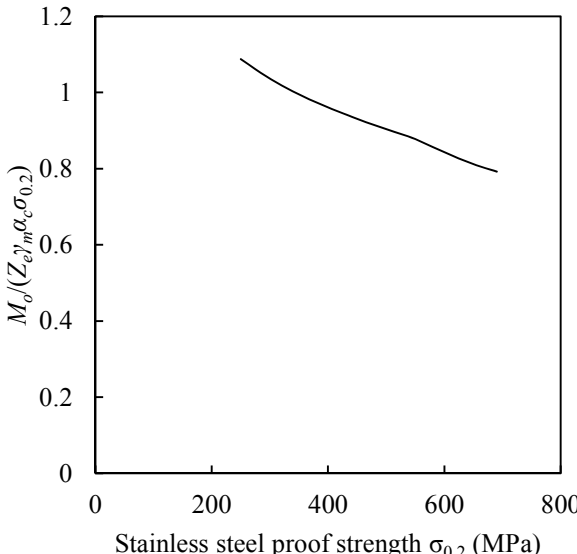
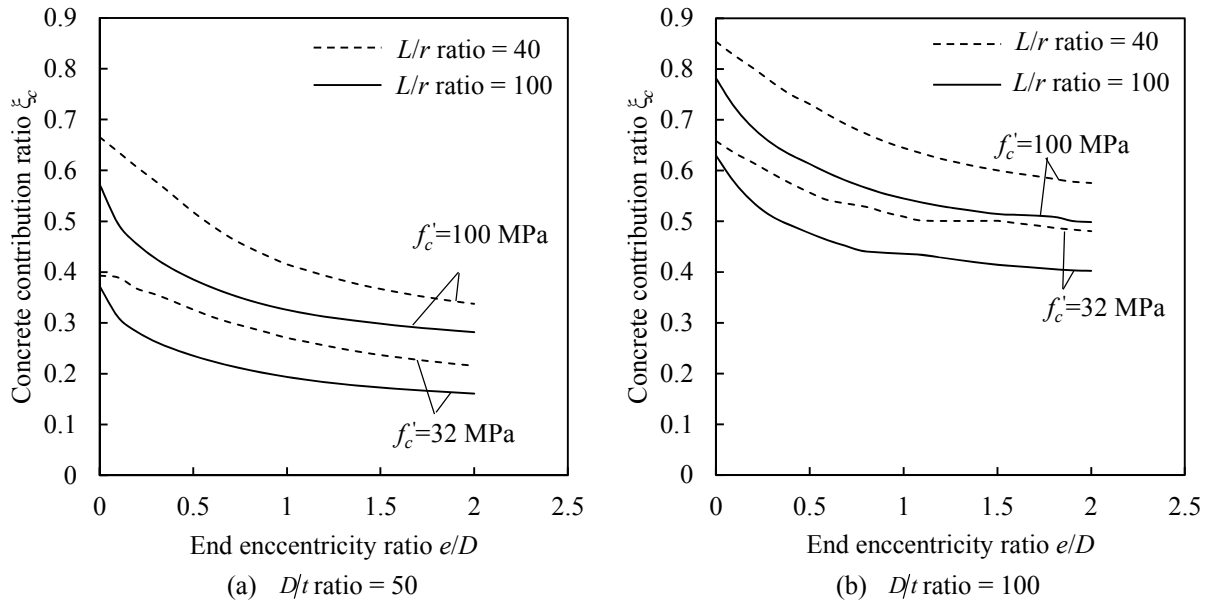**Fig. 12.** Influences of stainless steel proof stress $\sigma_{0.2}$ on the ultimate pure moment.

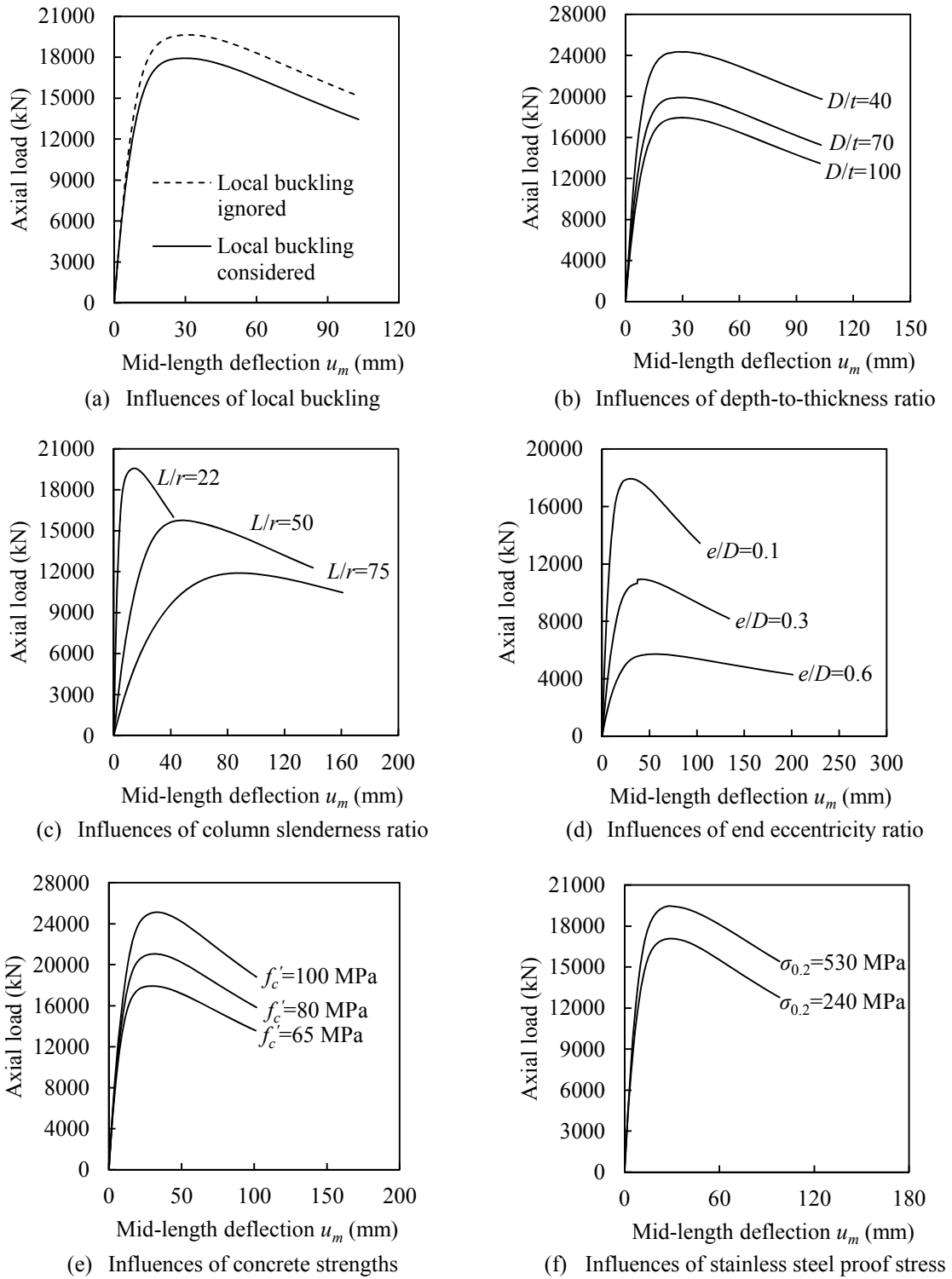**Fig. 13.** Influences of geometric and material parameters on the concrete contribution ratio.

(a) Influences of local buckling

(b) Influences of depth-to-thickness ratio

(c) Influences of column slenderness ratio

(d) Influences of end eccentricity ratio

(e) Influences of concrete strengths

(f) Influences of stainless steel proof stress

Fig. 14. Load-deflection behaviour of CFSST slender beam-columns with various geometric and material parameters.

(a) Column strength curves

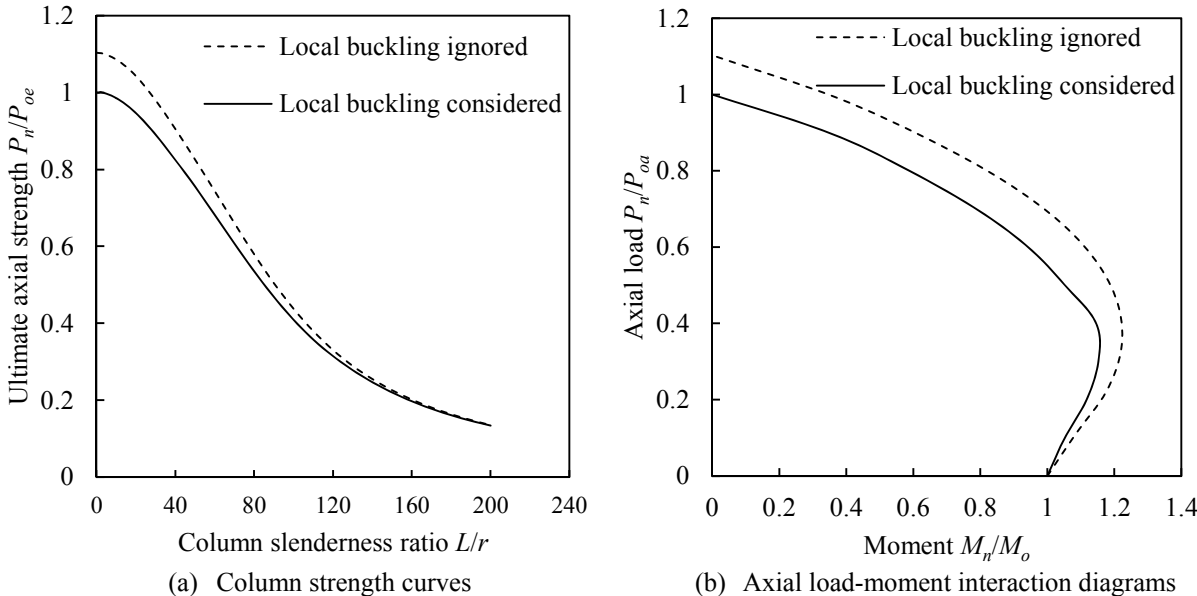(b) Axial load-moment interaction diagrams

Fig. 15. Influences of local buckling on the strengths of CFSST beam-columns.
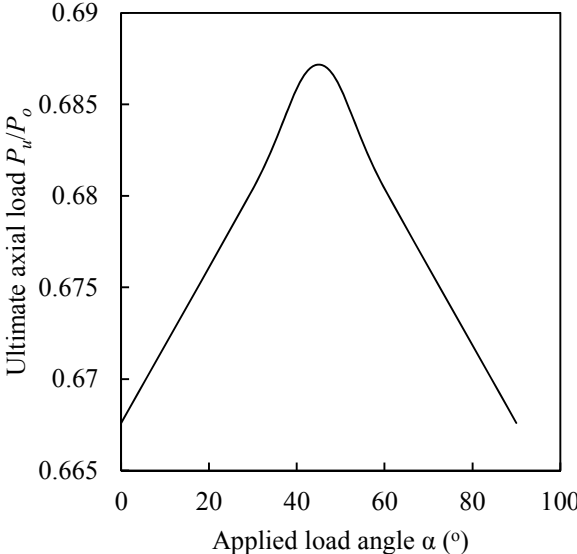

Fig. 16. Effects of the applied load angle on the ultimate load of CFSST beam-column.